Title

Anisotropic and curved lattice members enhance the structural integrity and mechanical performance of architected metamaterials

Authors

Vangelatos, Z
Komvopoulos, K
Spanos, J
et al.

Publication Date

2020-06-01

DOI

10.1016/j.ijsolstr.2020.02.023

Peer reviewed

International Journal of Solids and Structures 193–194 (2020) 287–301

Contents lists available at ScienceDirect

International Journal of Solids and Structures

journal homepage: www.elsevier.com/locate/ijsolstr

Anisotropic and curved lattice members enhance the structural integrity and mechanical performance of architected metamaterials

Z. Vangelatos [a], K. Komvopoulos [a,*], J. Spanos [b], M Farsari [b], C. Grigoropoulos [a,*]

[a] Department of Mechanical Engineering, University of California, Berkeley, CA 94720, USA
[b] Institute of Electronic Structure and Laser (IESL), Foundation of Research and Technology, Hellas (FORTH), Heraklion 70013, Crete, Greece

ARTICLE INFO

Article history:
Received 10 July 2019
Revised 12 February 2020
Accepted 12 February 2020
Available online 17 February 2020

Keywords:
Anisotropy
Architected structures
Controlled buckling
Deformation
Intertwined lattices
Mechanical metamaterials
Microlattice intertwining
Post-contact behavior
Unit cell

ABSTRACT

Architected metamaterials exhibit unique properties bestowed by their engineered structure rather than their chemical composition. Extrinsic material properties have been achieved as a result of advances in additive manufacturing. Contemporary fabrication techniques, such as multiphoton lithography and digital light processing, have enabled the fabrication of complex structures with inherent hierarchies at length scales ranging from nanometers to micrometers. However, despite significant insight into the role of buckling in the mechanical behavior of materials reported in earlier studies, particularly strength and energy dissipation, the structural and design principles responsible for the improved mechanical performance were not fully elucidated, thus limiting the design space of these structures. The principal objective of this study was to investigate how controlled three-dimensional assembly and orientation of intertwined lattice members influence localized buckling and the overall mechanical response of such metamaterial structures. The novelty of the present design approach stems from a mechanical metamaterial inspired by the three-compound octahedron and the symmetry variance observed during phase change of crystalline solids. For a specific orientation and tactical joining of the unit cells, this geometry demonstrates unprecedented resilience to large deformations and high energy dissipation capacity. The selective shape modification of specific lattice members is shown to greatly improve the structural integrity of ultralight structures undergoing large deformation. Results from finite element simulations and in situ scanning electron microscopy-microindentation experiments reveal the actual deformation of metamaterial structures with straight and curved lattice members and elucidate the effects of anisotropy and orientation characteristics on the dominant mechanisms affecting the mechanical performance of intertwined lattice structures.

1. Introduction

The design of novel structural metamaterials with unique properties is a principal scientific challenge. The fabrication of flexible structures with tailored mechanical properties is of critical importance in many application areas spanning a wide range of length scales, such as aerospace (Cramer et al., 2019), bioengineering (Brigo et al., 2017; Warner et al., 2017; Bobbert et al., 2018; Koffler et al., 2019), and microelectromechanical systems (Liu et al., 2014; Jayne et al., 2018; Ling et al., 2018). Ultralight-ultrastiff materials (Meza et al., 2014, 2017; Giorgio et al., 2017) and metamaterials with auxetic properties (Babaee et al., 2013; Warner et al., 2017; Wu et al., 2018a; Zhang et al., 2018) exhibit high deformation resilience and energy dissipation capacity, which are imperative characteristics for contemporary functional materials. The demonstrated potential of mechanical metamaterials has motivated exploratory studies dealing with controlled deformation of structures, such as pantographic structures (dell'Isola et al., 2016), tailored wave propagation (Fraternali et al., 2012; Berezovski et al., 2018), and microscale actuation (Zheludev and Plum, 2016; Jackson et al., 2018; Hippler et al., 2019). The vast majority of these designs have been inspired by nature (Wu et al., 2018b), deformation processes in natural materials, such as dislocations (Paulose et al., 2015a, 2015b) and damage in architected materials resembling crystal microstructures (Pham et al., 2019), or hierarchical structures of living organisms (Fratzl and Weinkamer, 2007; Yourdkhani et al., 2010). The fabrication of such complex structures with geometrical characteristics ranging from nanometers to millimeters has been principally achieved because of advances in additive man-

* Corresponding authors.
E-mail addresses: kyriakos@me.berkeley.edu (K. Komvopoulos), cgrigoro@me.berkeley.edu (C. Grigoropoulos).

https://doi.org/10.1016/j.ijsolstr.2020.02.023
0020-7683/

ufacturing techniques, including multiphoton lithography (MPL) (Ovsianikov et al., 2008), microstereolithoghraphy (Cui et al., 2018), and digital light processing (Schmidt and Colombo, 2018; Schmidt et al., 2019).

A critical factor in the design of novel mechanical metamaterials is the building blocks (unit cells) of the structure (Latture et al., 2018). Plate elements used to construct the unit cells of structures have been reported to yield significantly improved mechanical performance characterized by a stiffness approaching that of the bulk material (Berger et al., 2017). However, these unit cells have yet to surpass lattice structures that are still the predominant geometric features in metamaterial structures (Ashby, 2006). While the mechanical properties can be studied with three-dimensional (3D) beam models (Cazzani et al., 2016; Della Corte et al., 2019), simple two-dimensional (2D) models are still used to facilitate the understanding of experimental observations (Meza et al., 2014, 2017; Giorgio et al., 2017). Even though all of the above-mentioned fabrication techniques can produce highly complex 3D structures, the design space of mechanical metamaterials has been thoroughly studied only for 2D structures (Gibson and Ashby, 1997; Gao et al., 2018), while attempts to expand the design space of 3D structures, most notably auxetic mechanical metamaterials, have been recorded only recently (Chen et al., 2018). Hence, the design of ultralight-ultrastiff 3D lattice mechanical metamaterials has been limited to a few structures (Meza et al., 2017).

The mechanical response of complex 3D structures has been interpreted in the light of post-buckling behavior and intrinsic stiffening under compressive loading (Zadpoor and Hedayati, 2016; Latture et al., 2018); however, the structural principles for designing new unit cells have not been explored. Although different unit cells have been proposed for structures subjected to stretching and bending (Gibson and Ashby, 1997; Ashby, 2006), a comprehensive methodology for assembling unit cells is still lacking. This constraint becomes even more convoluted in the light of the anisotropic behavior of these structures and the limited insight into specific deformation modes (Giorgio et al., 2017). Another limitation is that force-displacement data have not been directly correlated to the true mechanical response and scale-dependent behavior of metamaterial structures (Meza et al., 2014, 2017; Gu and Greer, 2015). It is evident, therefore, that a link between size and geometry has not been established for mechanical metamaterial structures.

The objective of this investigation was to introduce a comprehensive design methodology for highly complex structures using geometrically simple elements. To this end, a novel mechanical metamaterial inspired by the isotropy groups in crystals undergoing phase change (Stokes and Hatch, 1988) was designed, fabricated, and tested. The geometry of the fabricated structures is based on the three-compound octahedron, a variation of the first stellation of the rhombic dodecahedron. The stellations of regular polyhedra provide basic geometries for an expanded and continuous design space (Coxeter et al., 1938). This is mainly due to the fact that the intertwining nature of multiple lattice members can be used to tailor buckling and stiffening. Two different paradigms of hierarchical assembly were considered in this study. As a design concept in nature, hierarchy depends on structural features existing at different scales of the same geometry (Meza et al., 2015; Fan et al., 2018). However, hierarchical patterns of the same length scale can simplify the fabrication process, hence significantly mitigating the complexity of the design process. Another principal objective of this study was to demonstrate how the structural integrity may be improved by modifying the lattice members of the metamaterial structure. Results from finite element simulations and in situ scanning electron microscopy-nanoindentation experiments are presented to elucidate the characteristic deformation stages of the fabricated metamaterial structures.

2. Design of anisotropic intertwined structures

2.1. Intertwined structures

The conceptual design process for assembling the architected metamaterial structures of this study is depicted in Fig. 1. The building blocks of the unit cell are three equilateral octahedra (Fig. 1(a)) with their edges connected in such a way that the intersection points divide each edge according to the $1{:}\sqrt{2}$ ratio (Fig. 1(b)). To obtain this geometrical arrangement, known as the three-compound octahedron (Cromwell, 1997), each octahedron is rotated by 45° with respect to the other two octahedra. It will be shown that such intertwining and positioning of lattice members in a confined space enables tailored buckling, which, in turn, enhances energy dissipation and contact of the buckled lattice members that causes structure stiffening. The reason for selecting this relative orientation of octahedra from a myriad of potential configurations is that this geometry has one symmetry group, i.e., octahedral symmetry (Shephard, 1999). Hence, the effect of the unit cell orientation on the deformation mode is drastically decreased. Nevertheless, it is not a uniform polyhedron compound, that is, transformations do not map every vertex to every other vertex; therefore, further intervention on the design process may alter the topology of the structure, e.g., the relative density or even the coordination number and, consequently, the mechanical properties (Shephard, 1999).

The potential design space is vast, considering there are 36 more isohedral deltahedra and many more stellations of regular polyhedra, such as the 59 stellations of the regular icosahedron (Coxeter et al., 1938). To further improve the mechanical performance, a second-level assembly was used in which neighboring unit cells were connected with each other; however, the symmetry of the formed hyper unit cell depends on the orientation of unit cells. Hence, different connections of unit cells may significantly affect the mechanical performance. In this study, the three-compound octahedron (Fig. 1(c)) was connected to the horizontal edges of neighboring unit cells in the horizontal plane (Fig. 1(d) and (e)) and the resulting hyper unit cell was used to assemble a three-layer structure (Fig. 1(f)). This design will be hereafter referred to as the design A. Alternatively, the three-compound octahedron was rotated by 45° (Fig. 1(g)), and the same process was used to form a hyper unit cell consisting of two three-compound octahedra connected to their vertices (Figs. 1(h) and 1(i)). The final structure was assembled by connecting the vertices of neighboring hyper unit cells (Fig. 1(j)). This design will be hereafter referred to as the design B. The reason for selecting these designs is that they represent two extreme cases from the connectivity perspective. In design A, each unit cell is connected to the edges of neighboring unit cells, whereas in design B, the unit cells are connected at their vertices. Therefore, the investigation of these two extreme designs may elucidate the effect of the present design process on the overall mechanical response (Bradley and Cracknell, 1972; Stokes and Hatch, 1988). Another reason for studying these designs is to unravel the effect of connectivity on the mechanical response. The particular design principle was inspired by the distortion of crystal symmetry during phase change in solids, which causes a variation in the mechanical response (Bradley and Cracknell, 1972).

At this juncture, it is instructive to categorize the structure as either bending or stretching dominated and compare its performance with characteristic architected materials from these families (Norris, 2014; Zadpoor and Hedayati, 2016). For this purpose, the average connectivity Z of the two designs was obtained by computing the number of beam elements and joints in each hyper unit cell (Deshpande et al., 2001). The average connectivity for designs A and B was found to be equal to 7 and 5, respectively. As both structures are 3D, a necessary and sufficient con-

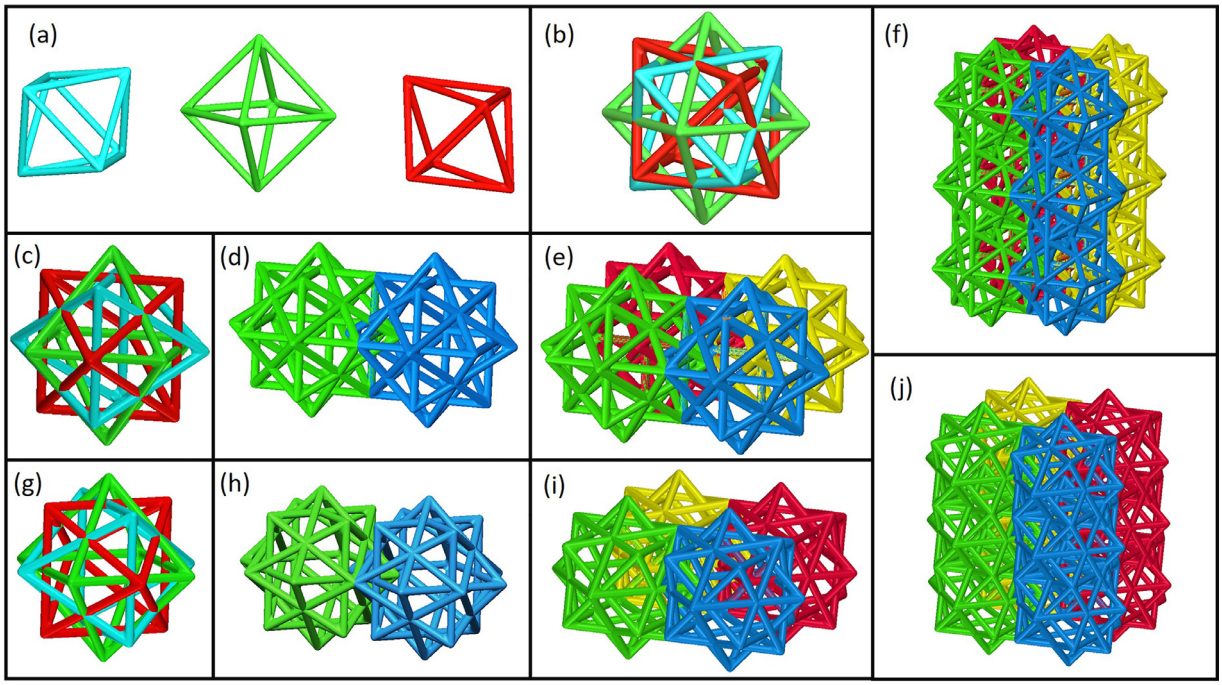

Fig. 1. The design process of anisotropic intertwined lattice structures with straight members. (a) Three regular octahedra are rotated clockwise and counter clockwise by 45° with respect to each other. (b) and (c) The three octahedra are assembled to form a three-compound octahedron unit cell. (d) Two unit cells are connected at their neighboring edges. (e) The same process is repeated in the normal direction to form a hyper unit cell (design A). (f) The final structure is assembled by connecting hyper unit cells in the vertical direction, creating a three-layer structure. (g) The unit cell shown in (b) rotated by 90° either clockwise or counter clockwise. (h)–(j) The process shown in (d)–(f) is used to create a three-layer structure by connecting hyper unit cells consisting of unit cells connected at their vertices (design B). The intertwining of lattice members enables tailored buckling and stiffening during deformation.

dition for the structures to be stretching dominated is $Z \geq 12$ (Norris, 2014). Therefore, these structures exhibit bending dominated behavior and belong to the same category of structures as the BCC, cube, diamond, Kelvin, and rhombic dodecahedron structures (Zadpoor and Hedayati, 2016).

According to the classical theory of the mechanical properties of foams and ultralight structures, the elastic stiffness, E, yield strength, σ_Y, and energy dissipation, u, depend on the relative density, $\bar{\rho}$, of the structure (Gibson and Ashby, 1997; Ashby, 2006; Meza et al., 2014, 2017). This property can be used to compare the mechanical properties of the unit cells. For the three-compound octahedron hyper unit cells with designs A and B, the relative density is given by

$$\bar{\rho}_A = 134.16\left(\frac{d}{L}\right)^2 - 699.12\left(\frac{d}{L}\right)^3 \quad (1)$$

and

$$\bar{\rho}_B = 121.96\left(\frac{d}{L}\right)^2 - 431.29\left(\frac{d}{L}\right)^3, \quad (2)$$

respectively, where d and L are the diameter and length of lattice members, respectively. The relative density of the structures for various values of the diameter/length ratio, d/L, was obtained with the 3D CAD design software (Solidworks 2016 × 64). To discount the effect of the excessive overlapping of the lattice members at the nodes from the relations of the relative density, the ends of the beams were cut with appropriately chosen cut surfaces in the CAD files and the results were then curve fitted to obtain Eqs. (1) and (2). The intertwining employed in design A may affect the relative density of the final structure compared to design B. The relative density corresponding to designs A and B is $\bar{\rho}_A \approx 0.248$ and $\bar{\rho}_B \approx 0.251$, respectively. These values were obtained from Eqs. (1) and (2) for $d = 0.5$ μm and $L = 10$ μm, which are the dimensions of the lattice members in the fabricated test structures. Although the difference in relative density is only 0.003, it will be shown that the strength and energy dissipation of the structures with designs A and B differ significantly. It is noted that the present 3D intertwining of only 12 unit cells yields very large relative densities. This can be ascertained by comparing the relative densities of the structures with designs A and B (Eqs. (1) and (2), respectively) with those of other thoroughly studied mechanical metamaterials (e.g., octet truss, cube, rhombic dodecahedron, diamond, Kelvin, and Weaire-Phelan) that have lattice members with circular cross sections (Hedayati et al., 2016; Zadpoor and Hedayati, 2016). In the equations of the relative density from the literature used for comparison, the overlapping of the lattice members at the nodes was also excluded from the calculated volume of these structures.

Fig. 2(a) shows the relative density of different unit cells as a function of the lattice diameter/length ratio. The significantly higher relative densities of the unit cells with designs A and B than those of other unit cells are attributed to their intrinsic intertwining, which becomes especially pronounced as d/L increases above 0.01. According to a previous study (Gong et al., 2005a), the estimated relative density of the Kelvin unit cell is also significantly lower than that of designs A and B in this range of d/L. To obtain the same relative density as in designs A and B, the diameter of each lattice member of the rhombic dodecahedron, for example, would have to be increased to 4 μm (Hedayati et al., 2016). However, this would greatly increase the fabrication time and the volume of the structure, making the mechanical performance mainly dependent on the bulk behavior, which is contrary to the main objective of this study to develop a design strategy effective in promoting localized buckling and overall stiffening. Importantly, the present design provides a means of enhancing the mechanical performance of structures in Ashby's charts (Meza et al., 2014, 2017) with a limited number of unit cells relative to conventional ultra-

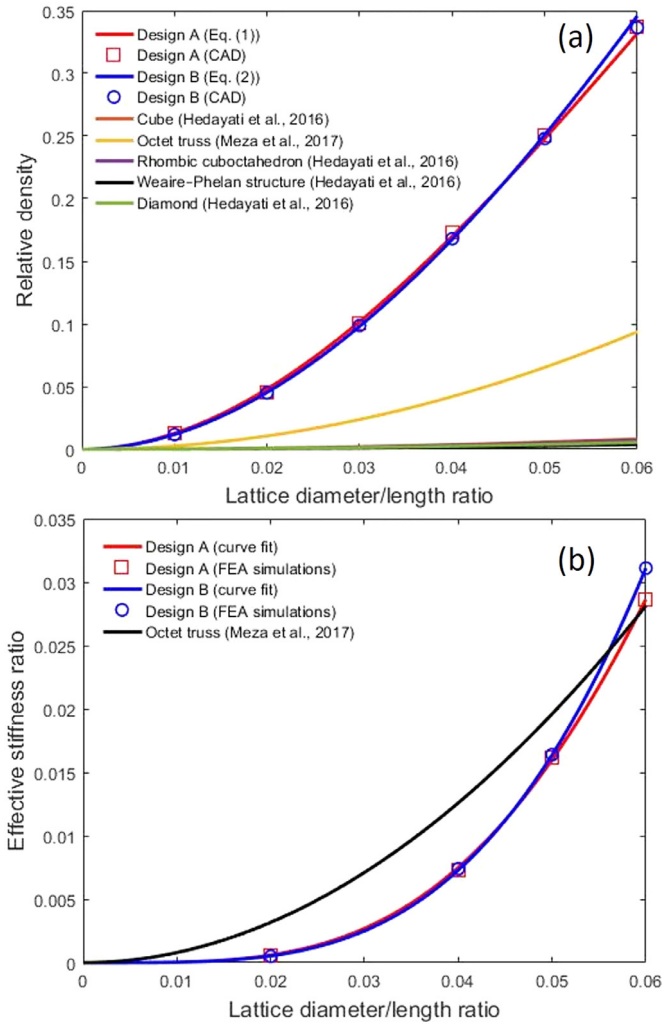

Fig. 2. Variation of the (a) relative density and (b) relative stiffness with the diameter/length ratio of lattice members in various unit cells. The 0–0.1 range of the diameter/length ratio is typical of the dimensions of structures fabricated by micro/nanolithography techniques. For this realm of dimensions, the structures with designs A and B show remarkably higher relative density compared to other bending dominated structures and higher relative stiffness than that of the octet truss structure for diameter/length ratios greater than 0.055.

light structures that do not utilize intertwining. A solid evidence of this effect can be obtained in the light of the results shown in Fig. 2(b). The effective stiffness $\bar{E}$ of the octet truss was plotted to follow the scaling law reported elsewhere (Meza et al., 2017), while the effective stiffness of the structures with designs A and B was plotted by curve fitting the data of FEA simulations performed for various d/L values and small normal displacements. The effective stiffness of bending dominated structures scales with the square of the relative density, whereas that of stretching dominated structures shows a linear scaling proclivity (Meza et al., 2017). While these power laws differ at high relative densities, the mechanical properties of bending and stretching dominated structures with $\bar{\rho} < 0.05$ can be accurately modeled by quadratic and linear scale laws, respectively. Although $\bar{\rho}_A$ and $\bar{\rho}_B$ are significantly larger than 0.05 (Fig. 2(a)), the quadratic scaling law fits closely the FEA data in the $0-0.06$ range of d/L (Fig. 2(b)). Even though the octet truss is stiffer in the range of $d/L < 0.055$, the remarkably higher relative density of the intertwined structures yields a stiffness of approximately the same order of magnitude as the octet truss for $d/L = 0.05$. At higher relative densities, even higher order terms (e.g., $(d/L)^4$) may have an additional contribution (Meza et al., 2017). However, since the present test structures are at the threshold of $d/L = 0.05$, their stiffness is comparable to that of stretching dominated structures. It is also noted that at higher d/L values, $\bar{\rho}_B$ begins to diverge from $\bar{\rho}_A$ significantly. Nevertheless, it will be shown that contact of beam members with neighboring members due to deformation is also critical to the mechanical behavior of the structure.

2.2. Curved lattice members

Another way to tailor the mechanical behavior of metamaterials is to use curved lattice members in certain locations of the structure. Introducing curvature in some lattice members can forestall deformation in specific directions (Cazzani et al., 2016), hindering deformation in other members as the stiffness will vary depending on whether the curved lattice members are convex or concave in the direction of loading. This design will be hereafter referred to as the design C (Fig. 3(a)). The curved red and blue lattice members were selected such that the structure to exhibit softening during loading, accordingly becoming more susceptible to large deformations. The curved members were placed where a unit cell was connected to neighboring unit cells (Fig. 3(b) and (c)), providing a union of connections for both edges and vertices. The assembled structure consisting of three layers of hyper unit cells is shown in Fig. 3(d). The coordination number of this structure is equal to 4, rendering it a bending dominated metamaterial structure as well. To enhance the deformability, the diameter of the lattice members was reduced to 0.25 μm, thereby increasing the slenderness ratio and, in turn, decreasing the critical load for buckling. The increase of the distance between the unit cells in the vertical direction yielded $\bar{\rho}_C = 0.023$, i.e., an order of magnitude less than $\bar{\rho}_A$ and $\bar{\rho}_B$. Despite the significantly reduced stiffness, it will be shown that this structure can sustain recoverable large deformations. Since this design is an alteration of design B, the curvature r of the curved lattice members leads to the following modification of Eq. (2), i.e.,

$$\bar{\rho}_C = f(r)\bar{\rho}_B. \tag{3}$$

For the specific configuration of design C, curve fitting of the relative densities corresponding to designs A and B obtained from the CAD models yielded $f(r) = 0.331$.

3. Modeling and experimental methods

3.1. Finite element analysis

A quasistatic finite element analysis (FEA) was performed to evaluate the mechanical response of the architected structures and to obtain preliminary insight into the anisotropy effect of the hyper unit cells on buckling and post-contact behavior. The FEA simulations were performed with the multi-physics code ANSYS (Workbench 18.0). The ANSYS Design Modeler was used to design the structure geometries. All of the beam members were discretized by 10-node, tetrahedral, finite elements. Surface contact was detected by 8-node surface elements assigned to the beam members of the top layer of the structure. The selected contact condition of the flat tip with the structures was no separation of the elements at the tip/structure contact interface. The structure with design A comprised 791,913 elements with 1283,397 nodes, the structure with design B had 937,285 elements with 1511,432 nodes, while the structure with design C was modelled with 332,721 elements having 635,257 nodes. Since the bottom face of each structure was firmly attached to a substrate, all the degrees of freedom of the bottom nodes were fully constrained. The base solid was modelled to have 0.5 GPa elastic modulus, 0.45 Poisson's ratio, and 18 MPa yield strength. These material properties are similar to those of the

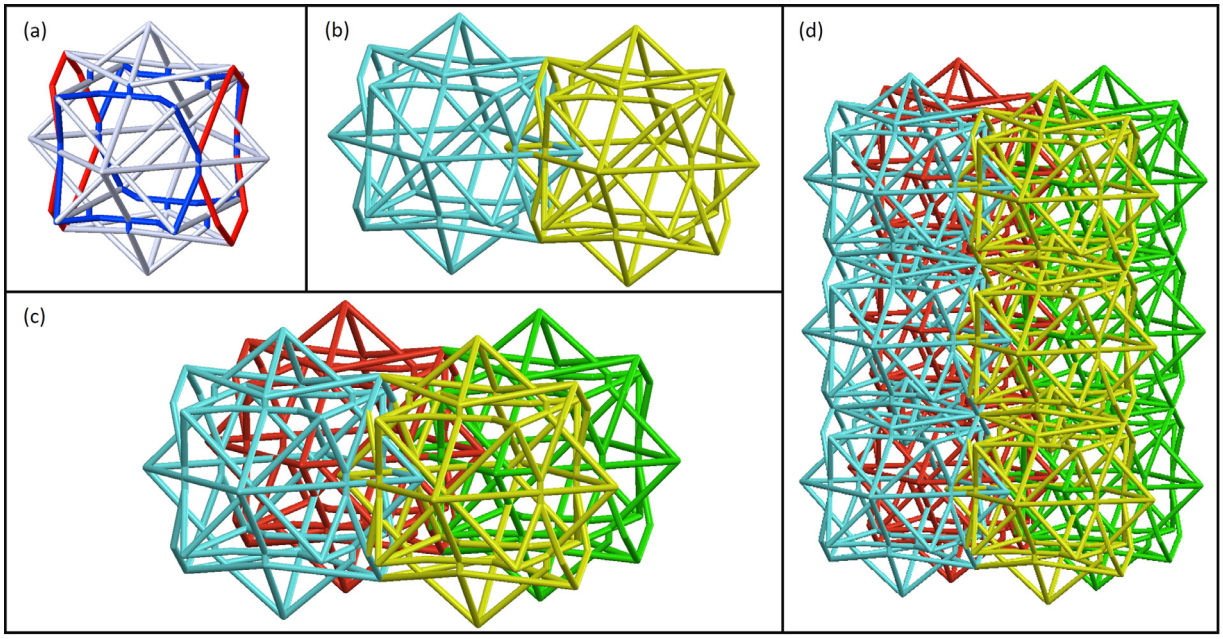

Fig. 3. The design process of anisotropic intertwined lattice structures with curved members. (a) The initial three-compound octahedron with curved lattice members coloured blue and red. (b) The assembly of two unit cells connected at their edges. (c) Two of the foregoing unit cells connected to two more unit cells at their vertices in the direction perpendicular to the direction the former unit cells were connected to their edges to allow larger deformation in a specific direction and to form a hyper unit cell. (d) The assembled final structure consisting of three layers of hyper unit cells (design C). The use of curved lattice members combined with strategic positioning of unit cells preserves the structural integrity even at large deformations.

polymers used in MPL fabrication. The tip was modeled to have 330 GPa elastic modulus, 0.29 Poisson's ratio, and 324 MPa ultimate tensile strength.

An eigenvalue buckling analysis was performed to investigate the buckling behavior of the structures. This was accomplished by solving the eigenvalue equation,

$$\det\left[[\boldsymbol{K}_{\sigma}[\sigma_0]]^{-1}[\boldsymbol{K}_{\boldsymbol{e}}]+\lambda\boldsymbol{I}\right]=0\ , \tag{4}$$

where $\boldsymbol{K}_{\sigma}$ is the initial stiffness matrix at a given stress state σ_0, calculated for the displacement field for incremental deformation, $\boldsymbol{K}_{\boldsymbol{e}}$ is the elastic stiffness matrix, and λ is a load multiplier, which is the solution of Eq. (4). The details of the derivation of Eq. (4) for 3D problems have been reported elsewhere (Krenk, 2009). Buckling commenced when the load applied to the structure reached a value equal to λ times a unit compressive load.

To extract engineering stress-strain responses from the experimental force-displacement curves, the tip-structure contact area was calculated as a function of tip displacement. The obtained numerical data were used to derive expressions of the contact area, which was then used to divide the measured force and compute the engineering stress. The engineering strain was calculated by dividing the tip displacement by the initial height of the structure. Any abrupt changes in contact of the beam members during the simulation were recorded by the FEA solver, enabling the post-contact events during the deformation to be enumerated. This result was also verified by visualizing the deformed configuration in the simulations.

3.2. Microfabrication

All of the test structures were fabricated by the MPL process, which uses multiphoton absorption to induce photoresist photopolymerization. The high spatial resolution provided by the MPL enables precise 3D fabrication (Sakellari et al., 2012). The MPL is particularly efficient for fabricating arbitrary 3D geometries compared to other techniques, such as fused deposition modeling or microstereolithography (Cui et al., 2018) requiring a very high resolution to fabricate complex structures. Moreover, the length scales achieved with the MPL provide structures that can be used for a plethora of fields, such as tissue bioengineering (Brigo et al., 2017; Maggi et al., 2017; Warner et al., 2017; Koffler et al., 2019) and microscale adaptive structures (Liu et al., 2014; Jayne et al., 2018; Ling et al., 2018; Lee et al., 2018).

The test structures were fabricated with an MPL apparatus equipped with a NIR laser (FemtoFiber pro, Toptica) of 780 nm wavelength, 100 fs pulse width, and 80 MHz repetition rate. The laser beam was focused by a 100 × microscope objective lens (Plan-ApoChromat 100 × /1.40 Oil M27, Zeiss). Localized polymerization of the structure material was achieved by tightly focusing the laser into the photosensitive material. The stage was translated so that the focused beam could 'write' inside the material and fabricate the desired structure. The structure beams were designed as lines oriented in a 3D space. This geometry was then converted to a g-code, whose coordinates defined the edges of the desired structure. Because the fabrication occurred from top to bottom, depending on the design of the structure, the geometry was designed to prevent line overlapping; otherwise the beam would interact with polymerized material. Further details about the experimental setup and materials used in the present study can be found elsewhere (Choi et al., 2018). The high resolution provided by MPL enables complex arbitrary structures to be produced by fabricating each individual lattice member in 3D space.

3.3. Mechanical testing

In situ indentation tests were performed with a nanoindentation apparatus (PI 85 SEM PicoIndenter, Hysitron) placed inside a scanning electron microscope (FEI Quanta 3D FEG), thus enabling high-precision nanomechanical testing and real-time recording of deformation. The molybdenum tip (Model # 72SC-D3/035 (407A-M)) was cut to a diameter of 130 μm with a femtosecond laser. The maximum tip displacement was set at 10 μm. A triangular force

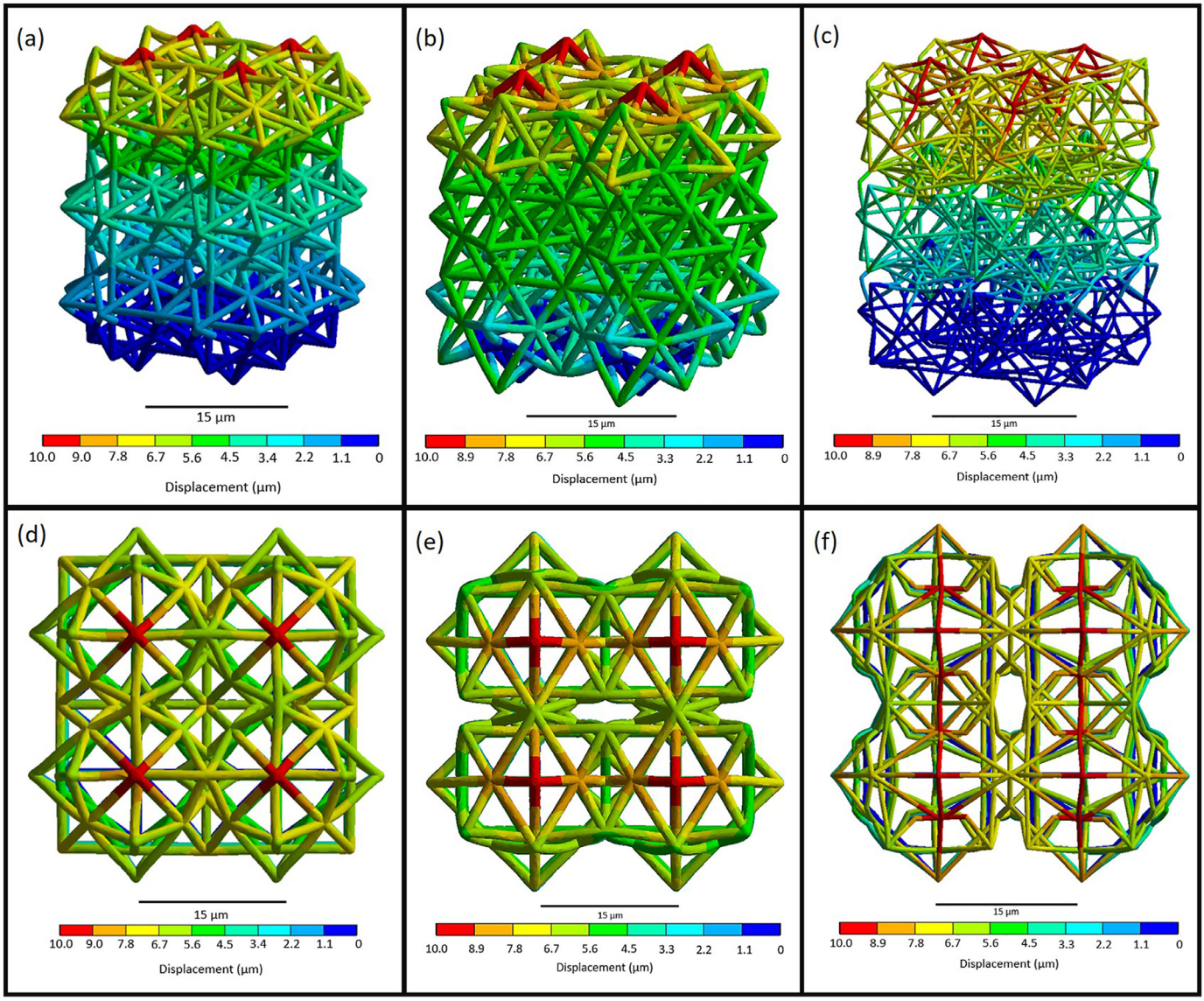

Fig. 4. FEA results of anisotropic intertwined lattice structures deformed in compression. Deformed structures with (a) design A, (b) design B, and (c) design C. Top-view of deformed structures with (d) design A, (e) design B, and (f) design C. Each structure consists of 12 unit cells with a height equal to 20 μm. The structure height in designs A, B, and C is 23, 20, and 48 μm, respectively. The simulations indicate that the lattice members of the upper layer (red colored) are most likely to fail first. The orientation of lattice members in design A lessens the deformation in the upper layer compared to the structure with design B. Because the structure with design C shares structural features common to both structures with designs A and B, deformation of the lower layers is minimal, while the largest deformation is sustained by the less supported lattice members of the upper layer.

function with loading and unloading rates both set at 0.2 μm/s was used in all the tests. To ensure the repeatability of the measurements, each experiment was repeated at least three times.

4. Results and discussion

4.1. Finite element simulations of metamaterial structures

Fig. 4 shows FEA simulation results of structures with designs A–C compressed by a flat tip. Each structure comprises three layers consisting of a 2×2 hyper unit cell (i.e., 12 unit cells). As expected, the largest deformation was sustained by the lattice members of the top layer of each structure (red colored). However, a comparison of Fig. 4(a) and (b) indicates that lattice intertwining in design A was significantly more effective in reducing deformation compared to design B, especially in the lattice members of the upper layer. This is attributed to the positioning of lattice members in the second stage of the assembly process of design A (Fig. 1(b)–(e)). Because the lattice members in design A that sustained most of the compressive deformation were much closer to each other, they contacted each other during deformation, increasing the structure's stiffness and strength. This result can be validated by considering the number of contacting beams (calculated at each of 1-μm-displacement steps) versus the tip displacement shown in Fig. 5. Design A shows a significantly larger number of beams in contact, with these post-contact events commencing at a smaller displacement (4 μm) compared to designs B and C (8 μm). As shown in the next section, the onset of post-contact at this early stage of deformation is critical to impeding microcracking through this intrinsic stiffening effect. Because the intertwined unit cells in design B (Fig. 1(g)–(i)) are connected with neighboring unit cells at their vertices rather than their edges, post-contact behavior was greatly mitigated. The lattice intertwining in design A also inhibited deformation of the lower layers (blue colored), whereas in design B

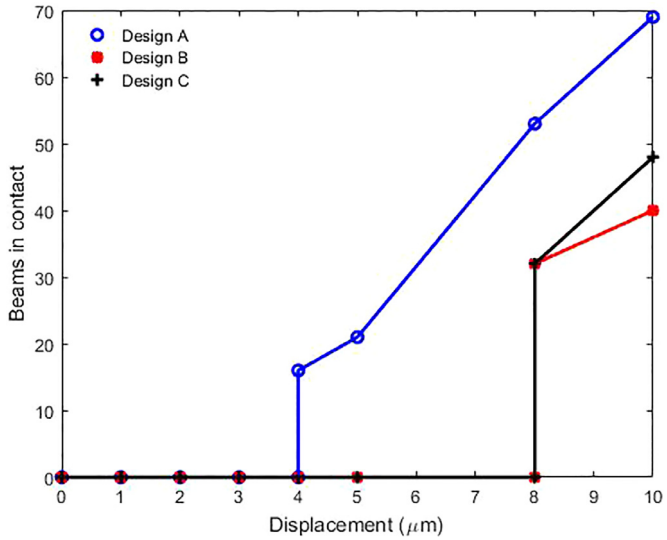

Fig. 5. Number of beam members coming into contact during deformation as a function of normal displacement. Post-contact of lattice elements in the structure with design A commences at a displacement of 4 μm as opposed to a much larger displacement of 8 μm for the structures with designs B and C.

all of the layers under the top layer exhibit fairly similar and relatively higher deformation (green colored). This intertwining also provides an energy dissipation mechanism in a multilayer structure. Interestingly, although the relative densities of designs A and B are approximately the same, the spatial orientation of the unit cells plays a critical role on the mechanical performance. The deformation encountered with design B was also observed with design C (Fig. 4(c)). This is attributed to the increased distance between lattice members. However, the connection of each unit cell to the edges mitigated the deformation in the lower layer, similar to what was observed with design A. The upper layers of each structure accrued most of the deformation, relaxing the rest of the structure. In particular, only eight of the top lattice members of the structure with design A sustained the largest deformation (Fig. 4(d)) as opposed to more lattice members in the structures with designs B and C (Fig. 4(e) and (f), respectively).

From the eigenvalue buckling analysis, the load multiplier ratio of designs A and B, λ_A/λ_B, was found to be equal to 1.08, implying essentially the same buckling load for both designs. Hence, structure anisotropy did not show a significant effect on buckling behavior. However, the load multiplier ratio of designs A and C, λ_A/λ_C, was found to be equal to 7.71, i.e., higher than λ_A/λ_B by a factor greater than 7. This indicates that curved lattice members can enhance buckling, provided they are positioned appropriately within the metamaterial structure.

Although the computed critical buckling loads provide insight into the overall instability of each structure, the experimental results presented below indicate that this buckling phenomenon is not associated with microscopic buckling instigated at the edges and walls of the unit cells (Haghpanah et al., 2014) and associated with the bifurcation instability of the beam members (Triantafyllidis and Maker, 1985). This localized buckling behavior is manifested at specific wavelengths that can be potentially larger than the dimensions of the unit cells (Haghpanah et al., 2014). These modes of the buckled structure, termed the representative volume element, demonstrate significant variance with each other, depending on the macroscopic loading conditions applied to the structure. These different modes can be obtained by methods like the Bloch wave theory (Geymonat et al., 1993; López Jiménez and Triantafyllidis, 2013). Moreover, metamaterial structures may also be subjected to macroscopic buckling or overall buckling, as reported for large wavelengths (Gibson et al., 1982; Gong and Kyriakides, 2005; Gong et al., 2005b; Okumura et al., 2007; Johnson et al., 2017). This behavior has been attributed to the loss of ellipticity of the homogenized incremental equilibrium equations of the material (Geymonat et al., 1993). Nevertheless, both of these effects are investigated and demonstrated under the assumption that the cellular structure extents infinitely in 3D space or for a specific number of unit cells that the solutions converge. Because the MPL can fabricate a small number of unit cells efficiently, the present study does not focus on these effects. Therefore, the critical buckling load and its corresponding mode may not be associated with long-wavelength instability of a large 3D structure and can only be interpreted in terms of the effect of instantaneous localized structural changes on the mechanical response observed in the experimental results of this study.

4.2. Fabricated metamaterial structures

Fig. 6 shows SEM images of three-layer metamaterial structures with designs A–C. The length and diameter of the lattice members of design A (Fig. 6(a) and (b)) and design B (Fig. 6(d) and (e)) is 10 and 0.5 μm, respectively, while the lattice members of design C (Fig. 6(c) and (f)) have a length of 10 μm and a diameter of 0.25 μm, which is the minimum diameter needed to preserve the structural integrity and prevent the collapse of the structure under its own weight. The dimensions of the unit cells shown in Fig. 6 are the same as those in the FEA simulations.

4.3. Mechanical behavior of metamaterial structures with straight lattice members

Fig. 7 shows a representative force versus displacement curve of the metamaterial structure with design A. The response comprises characteristic deformation stages labelled by A–E and shown in representative SEM images. The abrupt change in slope of the force-displacement response at a force of 1640 μN (point B) and 7060 μN (point C) is due to internal buckling of some lattice members, not fracture. The deformation behavior of this structure in the first load/unload cycle can be viewed in the video A of Supplemental Information (SI). The spontaneous decrease of the force slope at point B was instantly followed by a notable slope increase, attributed to structure stiffening due to the contact of buckled lattice members with other members. A similar buckling and post-contact sequence of events occurred at point C, i.e., before the maximum load was reached (point D). Importantly, the structure demonstrated significant recovery of its original configuration upon full unloading (point E), revealing a high resilience to large deformations and a unique capacity to dissipate strain energy by its intrinsic nonlinear deformation behavior.

Fig. 8 shows a typical force-displacement curve of the metamaterial structure with design B. The deformation behavior of this structure in the first load/unload cycle can be viewed in video B (SI). Although the characteristic deformation stages of the mechanical response are similar to those shown in Fig. 7, there is an important difference; that is, in addition to the two buckling events encountered at a load of 1401 μN (point B) and 5684 μN (point D), internal beam fracture occurred at a load of ~2000 μN (point C). The ratio of the loads corresponding to the first and second buckling events of designs A and B is equal to 1.17 and 1.24, respectively, which is in good agreement with the load multiplier ratio ($\lambda_A/\lambda_B = 1.08$) obtained from the eigenvalue buckling analysis. The inadequate support of the buckled lattice members due to limited post-contact with neighboring members led to fracture (point C), which continued to concurrently occur with further buckling (point D) as this structure lacked a crack arrest mechanism

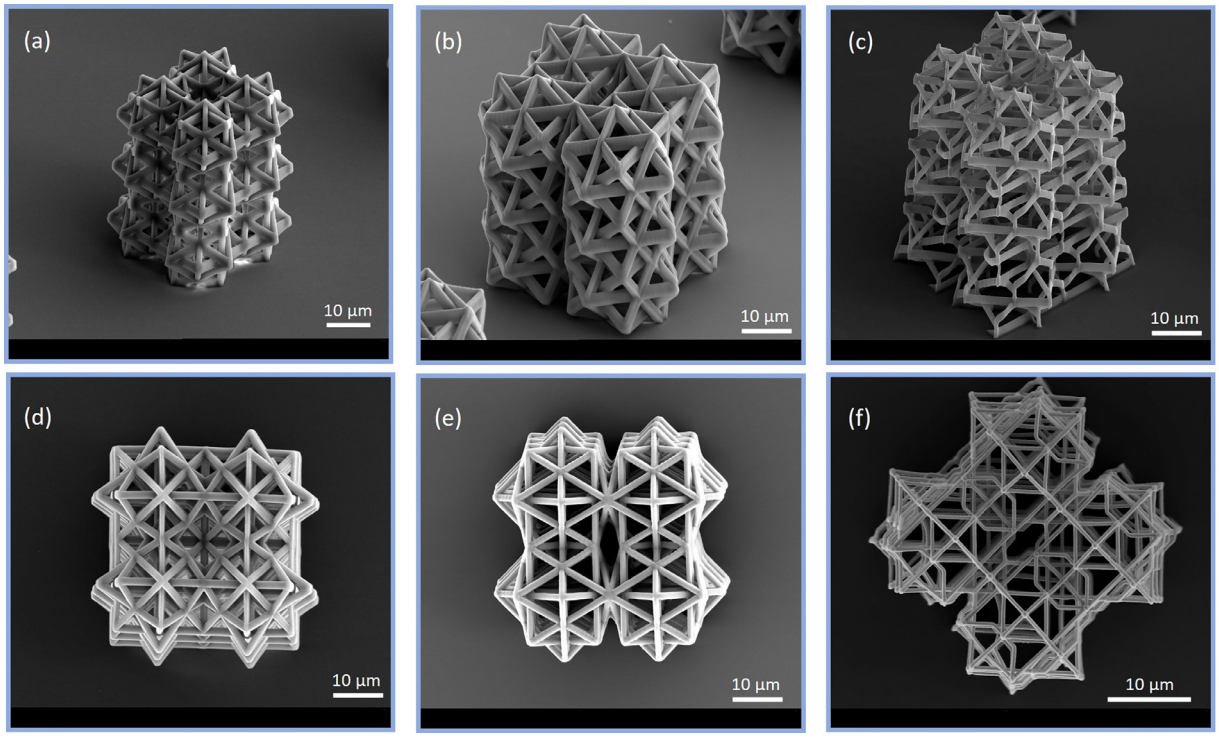

Fig. 6. SEM micrographs of anisotropic intertwined lattice structures with straight and curved members. Side view of structures with (a) design A, (b) design B, and (c) design C. Top view of structures with (d) design A, (e) design B, and (f) design C. The diameter of the lattice members in the structures with designs A and B is equal to 0.5 μm, while that of lattice members in the structure with design C is equal to 0.25 μm. The dimensions of unit cells are the same as those in the FEA simulations.

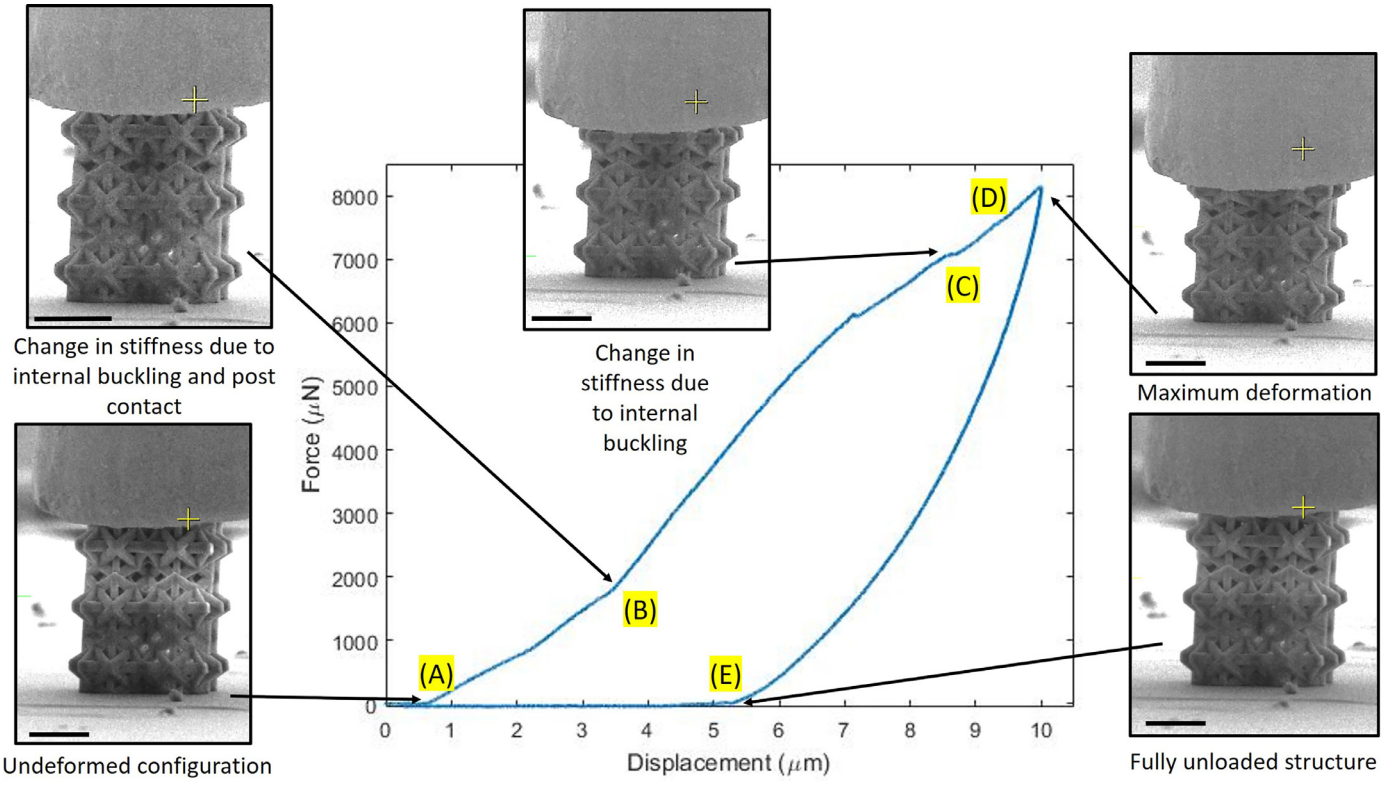

Fig. 7. In situ characterization of the mechanical performance of an anisotropic intertwined lattice structure with straight members (design A). The mechanical response comprises five distinct deformation states labelled by (A)–(E) and determined from the force versus displacement curve and the video A (SI) of the first load/unload cycle. The flat tip was first brought into contact with the structure (point A). A sudden change in the force slope occurred at a critical load (point B) due to internal buckling. However, the merely instantaneous increase of the slope indicates stiffening due to contact of lattice members with neighboring members. A second similar sudden change in slope occurred at a higher load (point C), suggesting further buckling and contact of lattice members before the maximum load was reached (point D). The original shape of the structure was fully recovered upon full unloading (point E) with only a minor damage accumulated in the lattice members of the top layer, indicative of the structure's resilience to large deformations and high strain energy absorption capacity. In all the SEM images, the bar scale is equal to 20 μm.

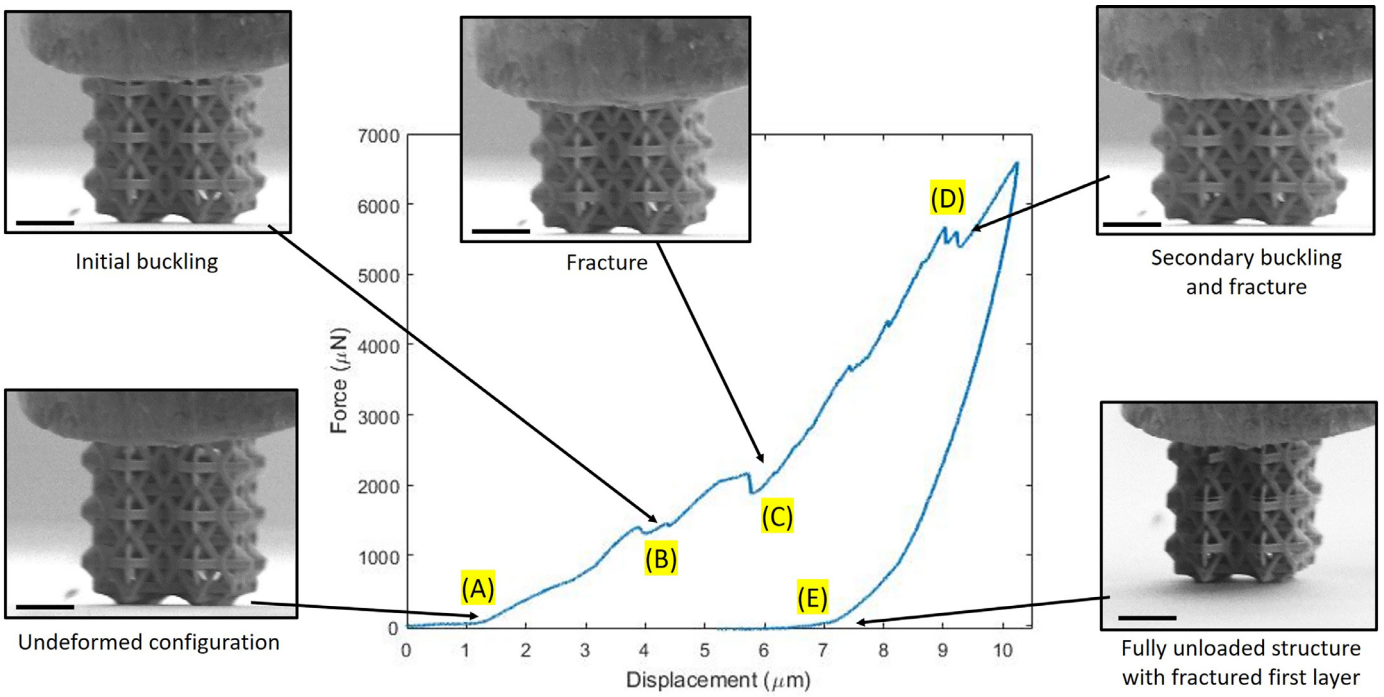

Fig. 8. In situ characterization of the mechanical performance of an anisotropic intertwined lattice structure with straight members (design B). The mechanical response comprises five distinct deformation states labelled by (A)–(E) and determined from the force versus displacement curve and the video B (SI) of the first load/unload cycle. After the engagement of the flat tip with the structure (point A), a sudden change in the force slope was encountered due to buckling of some lattice members (point B). However, in the absence of proximity lattice members to support the buckled members, fracture of buckled members was instigated with the further increase of the load (point C), and microfracture continued to evolve until the commencement of a second buckling event (point D) before the onset of unloading. The fully unloaded structure (point E) sustained extensive fracture of the lattice members in the top hyper unit cell. In all the SEM images, the bar scale is equal to 20 μm.

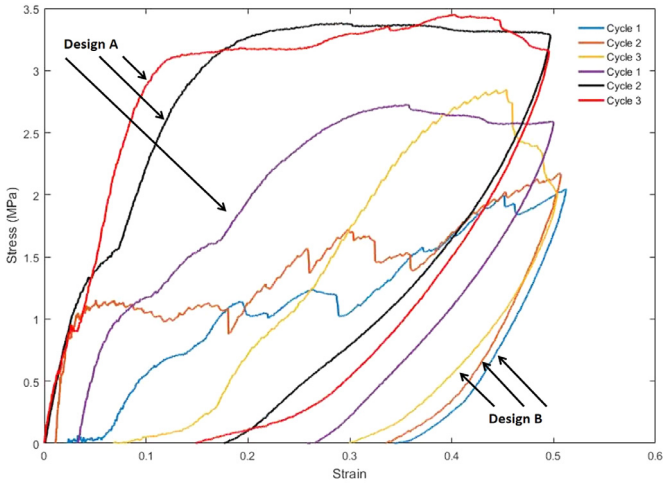

Fig. 9. Stress-strain responses of cyclically loaded anisotropic intertwined lattice structures with straight members (designs A and B). Three sequential load/unload cycles were applied to examine the dependence of the mechanical performance on the orientation of the unit cells. The results indicate commensurate augmentation of the stiffness, strength, strain hardening, and energy dissipation capacity of the structure with design A compared to that with design B, despite the similar relative densities and identical unit cells. The orientation of the unit cells in design A allowed post-contact of buckled lattice members, resulting in a more ductile-like behavior, whereas continuous fracturing of unsupported lattice members in the structure with design B produced a softening behavior.

(video B). Hence, design B does not meet the design objectives, despite having the same unit cell as design A.

To examine the evolution of the mechanical response due to cyclic loading, structures with designs A and B were subjected to three sequential load/unload cycles. The engineering stress-strain responses obtained from these experiments are shown in Fig. 9. For design A, energy dissipation (i.e., the force hysteresis area) increased initially and stabilized in the third cycle. Cyclic loading increased the slope of the loading curves of both structures, a consequence of contact between deformed and buckled lattice members. The stress drops in the loading response of the structure with design B in the first and second cycle are manifestations of multiple buckling and fracture events. In addition, the stress-strain response for design B reveals a brittle-like behavior that is devoid of the stress plateau observed with ductile materials and perpetual fracturing.

To further evaluate the mechanical performance of the foregoing structures, the residual strain, ε_r (obtained after full unloading), the energy dissipation per unit volume, u (i.e., the area under the stress-strain curve), and the elastic stiffness, S (i.e., the initial slope of the unloading curve), are compared in Table 1. The table includes statistical results obtained from all the cyclic loading tests. These results show that the structure with design A exhibits greater deformation resilience, significantly higher energy dissipation capacity, and much higher stiffness at each cycle compared to the structure with design B. In fact, the third-cycle results show ~2 times higher energy dissipation capacity and ~1.36 times higher stiffness for the structure with design A than that with design B. In addition, the rate of increase in energy dissipation is ~40% for the structure with design A and ~11.5% for the structure with design B, implying more significant strain hardening for the structure with design A, with the energy dissipation for the structure with design B also showing a decrease in the third cycle.

Another important difference is that the stress-strain responses corresponding to design A are fairly smooth, while those corresponding to design B show significant fluctuations during load-

Table. 1
Statistical data of the mechanical performance of anisotropic intertwined lattice structures with different designs versus load/unload cycle.

Load/unload cycle	Design A			Design B			Design C	
	ε_r	u (kJ/m^3)	S (MPa)	ε_r	u (kJ/m^3)	S (MPa)	ε_r	S (MPa)
1	0.210 ± 0.015	731.2 ± 15.5	41.21 ± 3.25	0.295 ± 0.055	446.6 ± 30.8	29.54 ± 5.83	0.153 ± 0.13	6.75 ± 0.25
2	0.150 ± 0.020	1022.3 ± 30.1	47.18 ± 3.91	0.277 ± 0.067	577.4 ± 45.9	36.82 ± 4.23	0.140 ± 0.13	9.45 ± 1.74
3	0.126 ± 0.030	1025.5 ± 45.2 (+40.2%)	49.72 ± 2.14 (+20.6%)	0.258 ± 0.075	497.8 ± 5.3 (+11.5%)	36.58 ± 1.09 (+23.8%)	0.134 ± 0.15	20.16 ± 4.91 (+198.7%)

*Numbers in parentheses indicate differences between the third and first cycle.

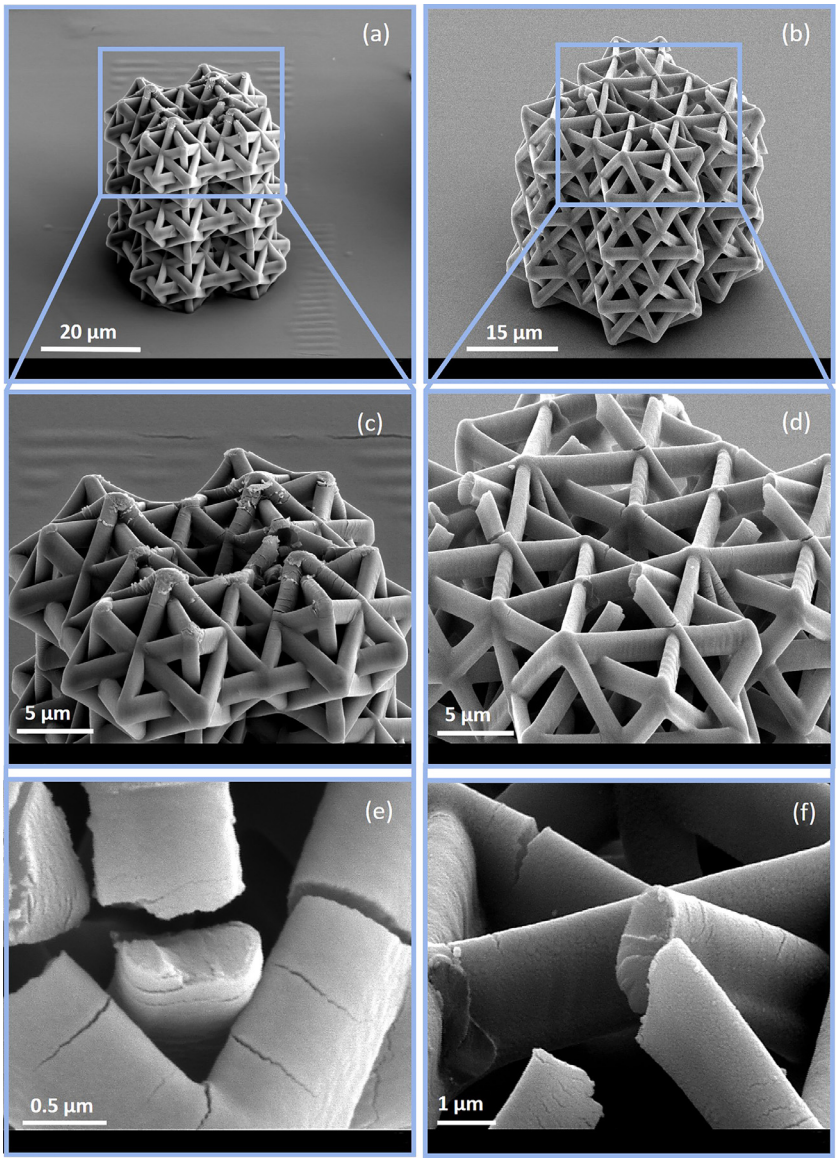

Fig. 10. SEM micrographs of anisotropic intertwined lattice structures with straight members obtained after three load/unload cycles. Side view of a damaged structure with (a) design A and (b) design B. High-magnification images showing fractured lattice members in the structures with (c) design A and (f) design B. The fractured lattice members correspond to the highly deformed lattice members shown in the FEA simulations. Post-contact of lattice members in design A halted crack growth, enhancing strain hardening and ductility. On the contrary, fracture was not inhibited in the structures with design B during loading in the first cycle due to the lack of post-contact of the buckled lattice members, resulting in a softening behavior. Highly deformed regions of structures with (e) design A and (f) design B. The relatively rough cross-sectional fracture areas of the lattice members of the structure with design A reveal ductile-like fracture, whereas the lines passing through the entire cross-sectional fracture area of the lattice members of the structure with design B reveal a multistage fracture process, demonstrating a transition from ductile-like to brittle-like fracture.

ing, indicative of perpetual fracture events. The mechanical responses shown in Fig. 9 reveal ductile-like deformation behavior for the structure with design A and brittle-like deformation behavior for the structure with design B. In the context of the developed stresses and deformations, the locations of the fractured lattice members (Fig. 10(a) and (b)) are consistent with the FEA simulation results, considering the maximum bending moments arise at the clamped ends of all beam members. Nevertheless, a comprehensive analysis of the fracture mechanisms requires a different FEA model, which is beyond the scope of the present study. The high-magnification micrographs of the highly damaged areas of metamaterial structures with designs A and B (Fig. 10(c)–(f))

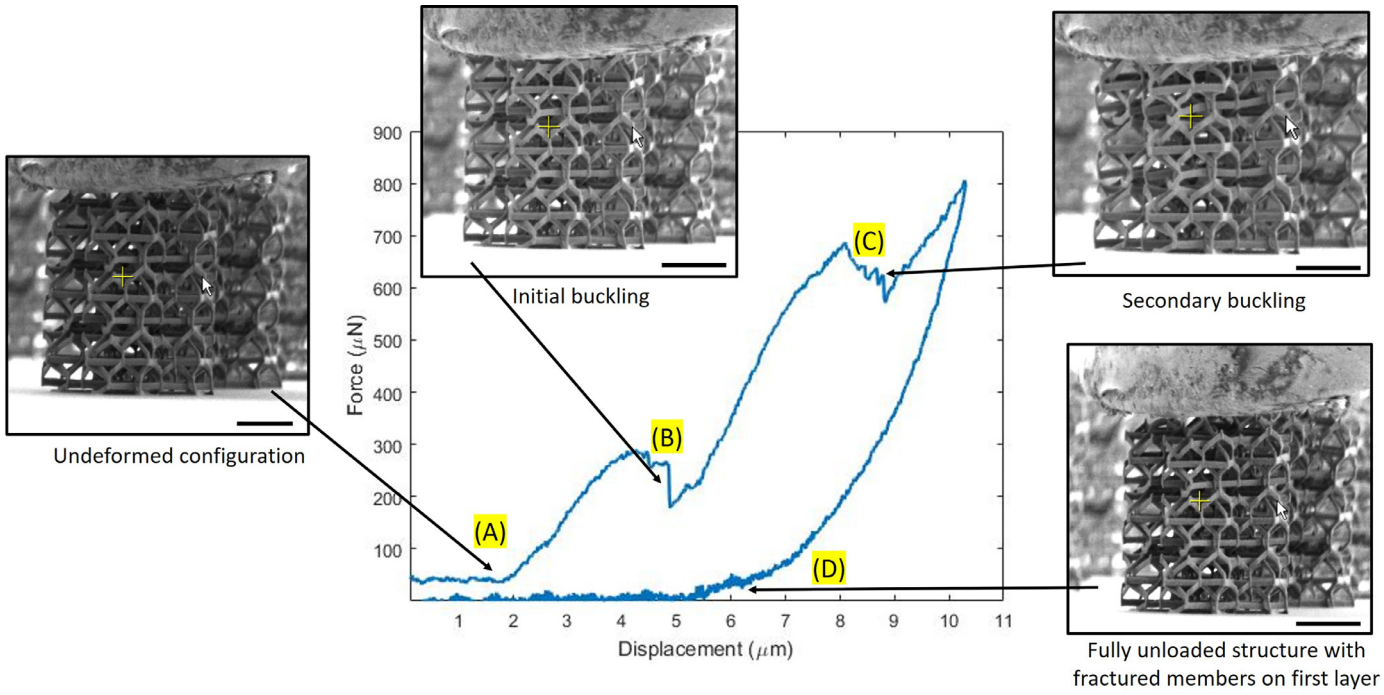

Fig. 11. In situ characterization of the mechanical performance of an anisotropic intertwined lattice structure with curved members (design C). The mechanical response comprises four distinct deformation states labelled by (A)–(D) and determined from the force versus displacement curve and the video C (SI) of the first load/unload cycle. During the loading of the original structure (point A), buckling of the lattice members of the top layer commenced (point B), followed by a second buckling event encompassing lattice members connecting the upper layer with the intermediate layer that resulted in tilting of the structure by ~30°. However, due to the capacity of the curved lattice members to sustain large deformations, the structure recovered its initial configuration upon full unloading (point D), despite fracturing of some lattice members of the top layer, consistent with the predictions of the FEA. In all the SEM images, the bar scale is equal to 20 μm.

provide further insight into the fracture of highly deformed lattice members. The areas containing the fractured lattice members (Fig. 10(c) and (d)) are the highly deformed areas predicted from the FEA simulations (Fig. 4). Because fewer buckled lattice members came into contact with other members in the structure with design B, this structure exhibited less deformation resistance compared to that with design A. In addition, Fig. 10(f) reveals a three-stage fracture process of the lattice members of the structure with design B, characterized by a transition from ductile-like to brittle-like fracture.

4.4. Mechanical behavior of metamaterial structures with curved lattice members

Fig. 11 shows a force-displacement curve characteristic of the structure with design C, and video C (SI) shows the deformation of this structure in the first load/unload cycle. Similar to the structure with design B (Fig. 8), this structure also exhibited two main buckling events at a load of 263 μN (point B) and 643 μN (point C). The load ratio corresponding to the first and third buckling events of designs A and C is equal to 6.23 and ~11, respectively. The difference between both of these values and the load multiplier ratio ($\lambda_A/\lambda_C = 7.71$) obtained from the eigenvalue buckling analysis is attributed to structural imperfections and the possible misalignment of the structure relative to the tip. Despite the large deformation sustained by this structure after each buckling event, its original configuration was fully recovered upon unloading (point D), also seen in video C (SI).

To study the evolution of the stress-strain response of this metamaterial structure, the deformation response after each of three consecutive load/unload cycles was examined with the SEM. Fig. 12 shows undeformed, highly deformed (maximum deformation), and fully unloaded configurations of the structure with design C for each loading cycle, whereas Fig. 13 shows the corresponding stress-strain responses. Cyclic loading produced similar buckling events in each cycle (videos C–E in SI), and the original configuration of the structure was fully recovered after each unloading. Although differences in macroscopic deformation were not detected with the SEM, the loading history differed significantly from those of the structures with designs A and B. Instead of the distinct stress fluctuations that characterized each buckling event in the first cycle, the responses of the second and third cycles were affected by a strain localization mechanism, resembling a strain hardening behavior similar to that caused by shear band formation (Jang et al., 2012). This is indicated by the increase of both the stress and the unloading slope between the second and third cycle. While buckling may induce localized strain softening in bulk materials (Mistakidis et al., 1997), it is possible that this mechanism was triggered by localized fracture in the first cycle of this structure, considering that fracture did not occur in any of the following cycles. Hence, the structure with design C demonstrated a macroscopic buckling mechanism that entrenched the fluctuating loading response in the first cycle. In traditional softening, a steady plastic flow is reached and the stress remains constant (Chen and Schweizer, 2011). However, the stiffness of this metamaterial structure increased after cyclic loading due to post-contact of some lattice members of the unit cells in the upper and intermediate layers, as evidenced from the stress-strain responses of the second and third cycle (Fig. 13), and this effect was conducive to preserving the structural integrity of this structure at all cycles.

The recoverability of this structure compared to those of other designs can be interpreted in the context of the results given in Table 1. Although the structure with design C exhibited the lowest residual strain in the first two cycles, its intrinsic softening mechanism mitigated the higher energy dissipation in the first cycle propelled by buckling (Fig. 13); however, the structural integrity was

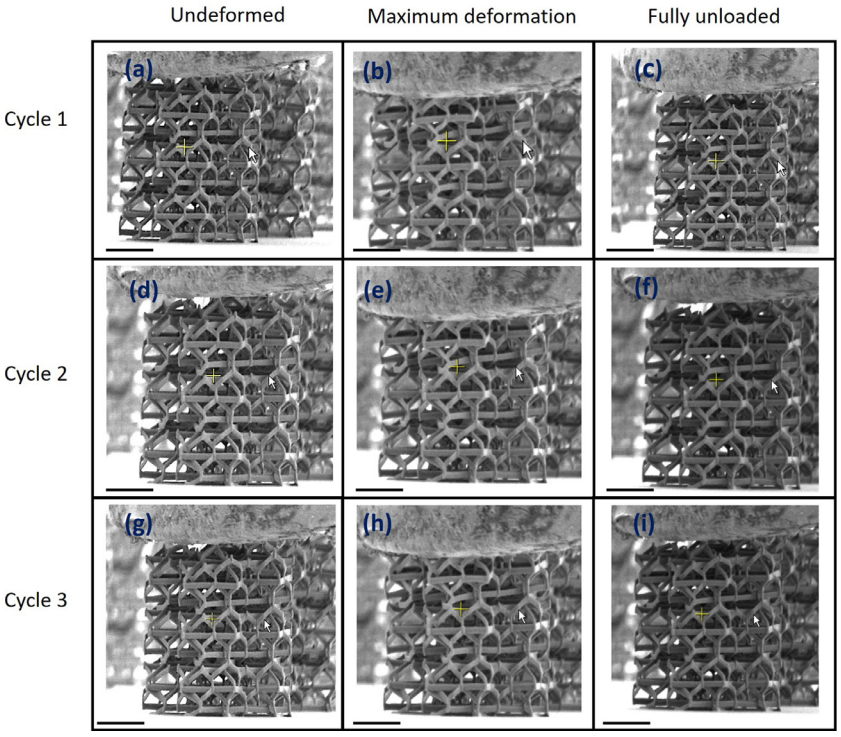

Fig. 12. SEM micrographs of an anisotropic intertwined lattice structure with curved members (design C) obtained after 1, 2, and 3 sequential load/unload cycles. (a) Undeformed, (b) highly deformed (maximum load), and (c) fully unloaded structure after the first cycle. (d) Undeformed, (e) highly deformed, and (f) fully unloaded structure after the second cycle. (g) Undeformed, (h) highly deformed, and (j) fully unloaded structure after the third cycle. Similar buckling events occurred in each loading cycle enabling the structures to fully recover their original configurations without fracture of any lattice member apart from a few lattice members of the top layer that fractured in the first cycle. In all the SEM images, the bar scale is equal to 20 μm.

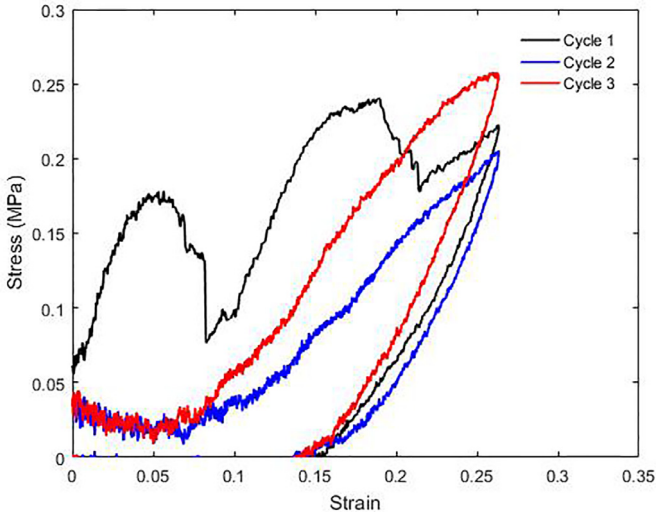

Fig. 13. Stress-strain responses of cyclically loaded anisotropic intertwined lattice structure with curved members (design C). Three sequential loading cycles were applied to examine the structural integrity of the structure. Despite the similar mechanical responses seen in videos C–E (SI) of the three cycles, localized buckling in the first cycle resulted in contact of lattice members of the top and intermediate layers, causing a significant stiffness increase in the second and third cycles.

not affected and further fracture of lattice members did not occur. Interestingly, in the third cycle the stiffness increased by ~200% from the first cycle, a result attributed to the large deformation of lattice members connecting the intermediate layer with the top layer, causing a variance in stiffness due to non-linear geometric effects (Cazzani et al., 2016; Della Corte et al., 2019). The highly deformed regions of this structure (Fig. 14) show that the cross-sectional fracture areas of lattice members comprise two regions – an external region at the perimeter of the member and an internal rough region. This morphology indicates that, despite the initial occurrence of instantaneous brittle fracture, the energy dissipation due to buckling transcended into ductile fracture at the later stage of crack growth.

The present study shows that the design of mechanical metamaterials with 3D intertwined lattice structures greatly enhances the stiffness, strain hardening/stiffening, and energy dissipation capacity. The employed design owes its effectiveness to the alignment of regular polyhedra in the 3D space and the use of a multilayer assembly method that not only increases the relative density of the structure, but also enhances buckling and post-contact of some lattice members. Importantly, it was confirmed that controlled buckling and post-contact, even for a small number of unit cells, do not exclusively depend on the relative density of the structure, but also on the strategic orientation of the unit cells and their connectivity with neighboring cells in the 3D space. Despite having identical unit cells, the hyper unit cells of the tested metamaterial structures differed in the connectivity of their unit cells. In design A, the unit cells were connected at their edges, while in design B the unit cells were connected at their vertices. Although post-contact of deformed lattice members was possible in both designs, this mechanism was not as effective in the structure with design B because the space between lattice members was not adequately utilized, leaving large areas unoccupied, hence resulting in post-contact of the deformed lattice members at much higher deformation. As a consequence, the buckled lattice members fractured because they lacked the contact support of neighboring members, resulting in softening and brittle behavior. Alternatively, design A comprised a stable core of intertwined lattice

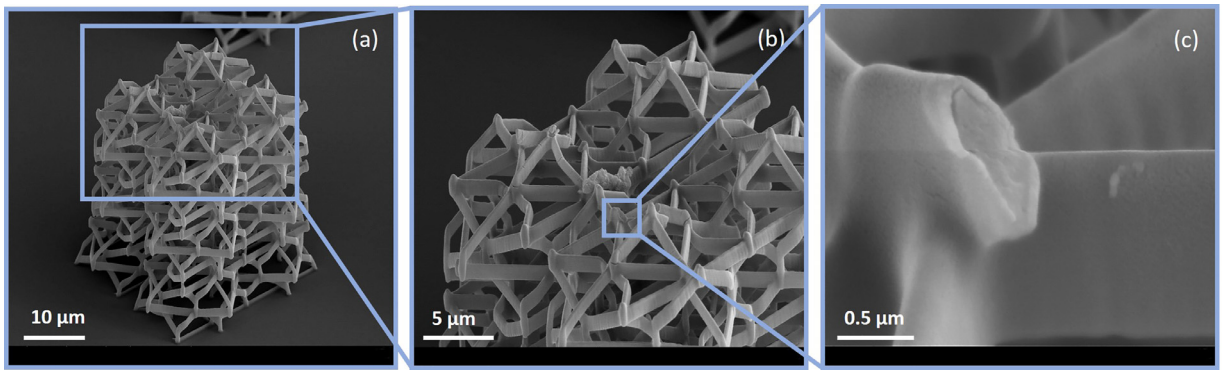

Fig. 14. SEM micrographs of fractured lattice members of an anisotropic intertwined lattice structure with curved members (design C) obtained after three sequential load/unload cycles. (a) Overall view of the highly deformed structure. (b) A fractured region of the top layer. (c) High-magnification image showing that the cross-sectional fracture area of lattice members comprises an external peripheral zone indicative of brittle-like fracture and an internal rough zone revealing ductile-like fracture.

members that exhibited post-contact upon buckling, which was validated by an FEA eigenvalue buckling analysis. This design principle is critical to the feasibility of intertwined lattice structures. The post-contact behavior was instrumental in yielding a ductile-like deformation behavior and enhancing the strain hardening and stiffness of the structure. Modifying the original unit cell by introducing curved lattice members (design C) enabled the metamaterial structure to sustain large reversible deformations. Despite the occurrence of softening that ameliorated the mechanical response by preventing buckling, this type of metamaterial structure fully recovered its undeformed configuration upon unloading. Using frame-by-frame visual examination and the force-displacement responses, buckling and fracture events were identified in all structures and the critical failure locations of lattice members were confirmed by FEA simulations.

The fact that the same relative density is not the only factor affecting the mechanical performance was demonstrated by the significant effects of the orientation and connectivity of the unit cells in the structures with designs A and B, despite the identical unit cells of these structures. Therefore, even slight changes in the configuration of the unit cell may result in a completely different geometry that must be addressed separately from all others. The direct consequence is the isolation of structures in the design space as independent entities and the means to efficiently navigate through the design space. In addition, because intertwined lattice structures combine both stretching and bending to enhance stiffening and energy dissipation, the classification of structures dominated explicitly by the former deformation modes is ambiguous. To address this issue, it is necessary to introduce a methodology that can identify isotropy subgroups in crystals. Furthermore, optimization tools, such as topology optimization (Thomsen et al., 2018) and deep learning (Ma et al., 2018), can be used to obtain an optimum configuration of intertwined unit cells. To this end, more advanced experimental techniques must be developed to effectively study anisotropy effects on metamaterial structures (Bauer et al., 2015). In addition, the MPL process must be advanced to facilitate the fabrication of novel and efficient structures for large-scale applications. Therefore, more systematic research is needed to integrate the MPL process with other techniques, such as holographic lithography (Campbell et al., 2000) or mesoscale fabrication (Jonušauskas et al., 2019), and expediting the design of versatile metamaterial structures for large-scale applications. Additionally, further investigation of both microscopic and macroscopic buckling phenomena is needed to reveal the effect of these mechanisms on large arrays of unit cells and the critical scale for convergence of the obtained modes. Because these structures are 3D and highly complex, optimization techniques, such as deep learning, may be effective in delineating these responses and finding the representative volume element.

5. Conclusions

A new design approach for mechanical metamaterials that provides significantly enhanced mechanical performance through tailored buckling and post-contact of some lattice members was introduced in this study. The basic geometry is the three-compound octahedron, a variation of the first stellation of the rhombic dodecahedron. The stellated geometries represent a vast source for the design space because they provide an abundance of different complex structures that can be systematically arranged to assemble hierarchical structures with each hierarchy level being at the same length scale. This is advantageous for overcoming the complexities introduced by the length scales needed to resemble the structural characteristics of biomimetic structures. Tailoring the unit cell orientation and shape can be accomplished through the effective integration of design principles, microfabrication, in situ mechanical characterization, and simulations, leading to either unprecedented or inconsistent mechanical behaviors. This study shows that tuning only the relative density and using standard design principles are inept for designing novel ultralight/ultrastiff architected structures.

Localized buckling and post-contact of lattice members provided a metamaterial structure with intertwined thick and straight members (design A) that showed increased resilience to large deformations, enhanced stiffness, and high energy dissipation capacity. However, keeping the same unit cell but changing the orientation of the unit cells in the structure degraded the mechanical performance due to fracture of the buckled lattice members (design B). Alternatively, the specific orientation and connectivity of the lattice members in the intermediate and top layers of the metamaterial structure with thin and curved members (design C) provided remarkable recoverability and high stiffness.

The unprecedented mechanical responses of structures with designs A–C were achieved by utilizing the connectivity and geometric effects of simple polyhedral structures. The present study establishes an important design foundation for architected metamaterials tuned to exhibit large reversible deformations, significant strain hardening/stiffening, and high energy dissipation capacity. This can be accomplished by controlling localized buckling of the lattice members and inducing ductile and strain localization responses that resemble those of bulk materials.

Declaration of competing interest

The authors declare that they have no known competing financial interests or personal relationships that could have appeared to influence the work reported in this paper.

CRediT authorship contribution statement

Z. Vangelatos: Conceptualization, Data curation, Formal analysis, Investigation, Methodology, Software, Validation, Visualization, Writing - original draft, Writing - review & editing. **K. Komvopoulos:** Conceptualization, Investigation, Supervision, Validation, Writing - original draft, Writing - review & editing. **J. Spanos:** Methodology. **M Farsari:** Resources. **C. Grigoropoulos:** Funding acquisition, Project administration, Resources, Supervision, Writing - review & editing.

Acknowledgments

The authors thank Professor P. Hosemann, Department of Nuclear Engineering, University of California, Berkeley, for using the microindetnation apparatus in his lab and his graduate students J. Kabel and H. Vo for training. The authors acknowledge A. Lemonis (IESL/FORTH) for assistance with the MPL software, V. Melissinaki (IESL/FORTH) for advice for the fabrication of the structures, and M. Park for helping with the fabrication of the nanoindentation tip. This research was partially supported by the National Science Foundation (NSF) under the Scalable Nanomanufacturing (SNM) Program, Grand No. 1449305.

Supplementary materials

Supplementary material associated with this article can be found, in the online version, at doi:10.1016/j.ijsolstr.2020.02.023.

References

Ashby, M.F., 2006. The properties of foams and lattices. Phil. Trans. R. Soc. A 364, 15–30.
Babaee, S., Shim, J., Weaver, J.C., Chen, E.R., Patel, N., Bertoldi, K., 2013. 3D soft metamaterials with negative Poisson's ratio. Adv. Mater. 25, 5044–5049.
Bauer, J., Schroer, A., Schwaiger, R., Tesari, I., Lange, C., Valdevit, L., Kraft, O., 2015. Push-to-pull tensile testing of ultra-strong nanoscale ceramic–polymer composites made by additive manufacturing. Extrem. Mech. Lett. 3, 105–112.
Berezovski, A., Yildizdag, M.E., Scerrato, D., 2018. On the wave dispersion in microstructured solids. Cont. Mech. Thermodyn doi:10.1007/s00161-018-0683-1.
Berger, J.B., Wadley, H.N.G., McMeeking, R.M., 2017. Mechanical metamaterials at the theoretical limit of isotropic elastic stiffness. Nature 543, 533–537.
Bobbert, F.S.L., Janbaz, S., Zadpoor, A.A., 2018. Towards deployable meta-implants. J. Mater. Chem. B 6, 3449–3455.
Bradley, C.J., Cracknell, A.P., 1972. The Mathematical Theory of Symmetry in Solids. Clarendon Press, Oxford, UK, pp. 7–22.
Brigo, L., Urciuolo, A., Giulitti, S., Giustina, G.D., Tromayer, M., Liska, R., Elvassore, N., Brusatin, G., 2017. 3D high-resolution two-photon crosslinked hydrogel structures for biological studies. Acta Biomater. 55, 373–384.
Campbell, M., Sharp, D.N., Harrison, M.T., Denning, R.G., Turberfield, A.J., 2000. Fabrication of photonic crystals for the visible spectrum by holographic lithography. Nature 404, 53–56.
Cazzani, A., Malagù, M., Turco, E., Stochino, F., 2016. Constitutive models for strongly curved beams in the frame of isogeometric analysis. Math. Mech. Solids 21, 182–209.
Chen, K., Schweizer, K.S., 2011. Theory of yielding, strain softening, and steady plastic flow in polymer glasses under constant strain rate deformation. Macromolecules 44, 3988–4000.
Chen, D., Skouras, M., Zhu, B., Matusik, W., 2018. Computational discovery of extremal microstructure families. Sci. Adv. 4, eaao7005.
Choi, J., Koo, S., Sakellari, I., Kim, H., Su, Z., Carter, K.R., Farsari, M., Grigoropoulos, C.P., Russell, T.P., 2018. Guided assembly of block copolymers in three-dimensional woodpile scaffolds. ACS Appl. Mater. Interf. 10, 42933–42940.
Coxeter, H.S.M., Du Val, P., Flather, H.T., Petrie, J.F., 1938. The Fifty-Nine Icosahedra. The University of Toronto Press, Toronto, Canada, pp. 8–26.
Cramer, N.B., Cellucci, D.W., Formoso, O.B., Gregg, C.E., Jenett, B.E., Kim, J.H., Lendraitis, M., Swei, S.S., Trinh, G.T., Trinh, K.V., Cheung, K.C., 2019. Elastic shape morphing of ultralight structures by programmable assembly. Smart Mater. Struct. 28, 055006.
Cromwell, P.R., 1997. Polyhedra. Cambridge University Press, Cambridge, UK, p. 195.
Cui, H., Hensleigh, R., Chen, H., Zheng, X., 2018. Additive manufacturing and size-dependent mechanical properties of three-dimensional microarchitected, high-temperature ceramic metamaterials. J. Mater. Res. 33, 360–371.
Della Corte, A., Battista, A., dell'Isola, F., Seppecher, P., 2019. Large deformations of Timoshenko and Euler beams under distributed load. Z. Angew. Math. Phys. 70, 52.
dell'Isola, F., Giorgio, I., Pawlikowski, M., Rizzi, N.L., 2016. Large deformations of planar extensible beams and pantographic lattices: heuristic homogenization, experimental and numerical examples of equilibrium. Proc. R. Soc. A 472, 20150790.
Deshpande, V.S., Ashby, M.F., Fleck, N.A., 2001. Foam topology bending versus stretching dominated architectures. Acta Mater. 49, 1035–1040.
Fan, H., Luo, Y., Yang, F., Li, W., 2018. Approaching perfect energy absorption through structural hierarchy. Int. J. Eng. Sci. 130, 12–32.
Fraternali, F., Senatore, L., Daraio, C., 2012. Solitary waves on tensegrity lattices. J. Mech. Phys. Solids 60, 1137–1144.
Fratzl, P., Weinkamer, R., 2007. Nature's hierarchical materials. Prog. Mater. Sci. 52, 1263–1334.
Gao, Z., Liu, D., Tománek, D., 2018. Two-dimensional mechanical metamaterials with unusual Poisson ratio behavior. Phys. Rev. Appl. 10, 064039.
Geymonat, G., Müller, S., Triantafyllidis, N., 1993. Homogenization of nonlinearly elastic materials, microscopic bifurcation and macroscopic loss of rank-one convexity. Arch. Rational Mech. Anal. 122, 231–290.
Gibson, L.J., Ashby, M.F., 1997. Cellular Solids: Structure and Properties. 2nd ed. Cambridge University Press, Cambridge, UK, pp. 341–386.
Gibson, L.J., Ashby, M.F., Schajer, G.S., Robertson, C.I., 1982. The mechanics of two-dimensional cellular materials. Proc. R. Soc. A 382, 25–42.
Giorgio, I., Rizzi, N.L., Turco, E., 2017. Continuum modelling of pantographic sheets for out-of-plane bifurcation and vibrational analysis. Proc. R. Soc. A 473, 20170636.
Gong, L., Kyriakides, S., Jang, W.-Y., 2005a. Compressive response of open-cell foams. Part I: Morphology and elastic properties. Int. J. Solids Struct. 42, 1355–1379.
Gong, L., Kyriakides, S., Triantafyllidis, N., 2005b. On the stability of Kelvin cell foams under compressive loads. J. Mech. Phys. Solids 53, 771–794.
Gong, L., Kyriakides, S., 2005. Compressive response of open cell foams. Part II: Initiation and evolution of crushing. Int. J. Solids Struct. 42, 1381–1399.
Gu, X.W., Greer, J.R., 2015. Ultra-strong architected Cu meso-lattices. Extem. Mech. Lett. 2, 7–14.
Haghpanah, B., Papadopoulos, J., Mousanezhad, D., Nayeb-Hashemi, H., Vaziri, A., 2014. Buckling of regular, chiral and hierarchical honeycombs under a general macroscopic stress state. Proc. R. Soc. A 470, 20130856.
Hedayati, R., Sadighi, M., Mohammadi-Aghdam, M., Zadpoor, A.A., 2016. Effect of mass multiple counting on the elastic properties of open-cell regular porous biomaterials. Mater. Des. 89, 9–20.
Hippler, M., Blasco, E., Qu, J., Tanaka, M., Barner-Kowollik, C., Wegener, M., Bastmeyer, M., 2019. Controlling the shape of 3D microstructures by temperature and light. Nature Commun. 10, 232.
Jackson, J.A., Messner, M.C., Dudukovic, N.A., Smith, W.L., Bekker, L., Moran, B., Golobic, A.M., Pascall, A.J., Duoss, E.B., Loh, K.J., Spadaccini, C.M., 2018. Field responsive mechanical metamaterials. Sci. Adv. 4, eaau6419.
Jang, D., Li, X., Gao, H., Greer, J.R., 2012. Deformation mechanisms in nanotwinned metal nanopillars. Nat. Nanotechnol. 7, 594–601.
Jayne, R.K., Stark, T.J., Reeves, J.B., Bishop, D.J., White, A.E., 2018. Dynamic actuation of soft 3D micromechanical structures using micro-electromechanical systems (MEMS). Adv. Mater. Technol. 3, 1700293.
Johnson, C.G., Jain, U., Hazel, A.L., Pihler-Puzović, D., Mullin, T., 2017. On the buckling of an elastic holey column. Proc. R. Soc. A 473, 20170477.
Jonušauskas, L., Gailevičius, D., Rekštytė, S., Baldacchini, T., Juodkazis, S., Malinauskas, M., 2019. Mesoscale laser 3D printing. Opt. Express 27, 15205–15221.
Koffler, J., Zhu, W., Qu, X., Platoshyn, O., Dulin, J.N., Brock, J., Graham, L., Lu, P., Sakamoto, J., Marsala, M., Chen, S., Tuszynski, M.H., 2019. Biomimetic 3D-printed scaffolds for spinal cord injury repair. Nat. Med. 25, 263–269.
Krenk, S., 2009. Non-linear Modeling and Analysis of Solids and Structures. 1st ed. Cambridge University Press, Cambridge, UK, pp. 20–26.
Latture, R.M., Begley, M.R., Zok, F.W., 2018. Design and mechanical properties of elastically isotropic trusses. J. Mater. Res. 33, 249–263.
Lee, H.-T., Kim, M.-S., Lee, G.-Y., Kim, C.-S., Ahn, S.-H., 2018. Shape memory alloy (SMA)-based microscale actuators with 60% deformation rate and 1.6 kHz actuation speed. Small 14, 1801023.
Ling, Y., Zhuang, X., Xu, Z., Xie, Y., Zhu, X., Xu, Y., Sun, B., Lin, J., Zhang, Y., Yan, Z., 2018. Mechanically assembled, three-dimensional hierarchical structures of cellular graphene with programmed geometries and outstanding electromechanical properties. ACS Nano 12, 12456–12463.
Liu, K., Cheng, C., Suh, J., Tang-Kong, R., Fu, D., Lee, S., Zhou, J., Chua, L.O., Wu, J., 2014. Powerful, multifunctional torsional micromuscles activated by phase transition. Adv. Mater. 26, 1746–1750.
López Jiménez, F., Triantafyllidis, N., 2013. Buckling of rectangular and hexagonal honeycomb under combined axial compression and transverse shear. Int. J. Solids Struct. 50, 3934–3946.
Ma, W., Cheng, F., Liu, Y., 2018. Deep-learning-enabled on-demand design of chiral metamaterials. ACS Nano 12, 6326–6334.
Maggi, A., Li, H., Greer, J.R., 2017. Three-dimensional nano-architected scaffolds with tunable stiffness for efficient bone tissue growth. Acta Biomater. 63, 294–305.

Meza, L.R., Das, S., Greer, J.R., 2014. Strong, lightweight, and recoverable three-dimensional ceramic nanolattices. Science 345, 1322–1326.
Meza, L.R., Phlipot, G.P., Portela, C.M., Maggi, A., Montemayor, L.C., Comella, A., Kochmann, D.M., Greer, J.R., 2017. Reexamining the mechanical property space of three-dimensional lattice architectures. Acta Mater. 140, 424–432.
Meza, L.R., Zelhofer, A.J., Clarke, N., Mateos, A.J., Kochmann, D.M., Greer, J.R., 2015. Resilient 3D hierarchical architected metamaterials. Proc. Nat. Acad. Sci. USA 112, 11502–11507.
Mistakidis, E.S., Thomopoulos, K.T., Tzaferopoulos, M.Ap., 1997. Effective methods for the analysis of steel structures with strain-softening behaviour. J. Construct. Steel Res. 44, 3–21.
Norris, A.N., 2014. Mechanics of elastic networks. Proc. R. Soc. A 470, 20140522.
Okumura, D., Okada, A., Ohno, N., 2007. Long wavelength buckling of cubic open–cell foams subjected to uniaxial compression. Key Eng. Mater. 353-358, 583–586.
Ovsianikov, A., Viertl, J., Chichkov, B., Oubaha, M., MacCraith, B., Sakellari, I., Giakoumaki, A., Gray, D., Vamvakaki, M., Farsari, M., Fotakis, C., 2008. Ultra-low shrinkage hybrid photosensitive material for two-photon polymerization microfabrication. ACS Nano 2, 2257–2262.
Paulose, J., Meeussen, A.S., Vitelli, V., 2015a. Selective buckling via states of self-stress in topological metamaterials. Proc. Nat. Acad. Sci. USA 112, 7639–7644.
Paulose, J., Chen, B.G., Vitelli, V., 2015b. Topological modes bound to dislocations in mechanical metamaterials. Nat. Phys. 11, 153–156.
Pham, M.-S., Liu, C., Todd, I., Lertthanasarn, J., 2019. Damage-tolerant architected materials inspired by crystal microstructure. Nature 565, 305–311.
Sakellari, I., Kabouraki, E., Gray, D., Purlys, V., Fotakis, C., Pikulin, A., Bityurin, N., Vamvakaki, M., Farsari, M., 2012. Diffusion-assisted high-resolution direct femtosecond laser writing. ACS Nano 6, 2302–2311.
Schmidt, J., Colombo, P., 2018. Digital light processing of ceramic components from polysiloxanes. J. Europ. Ceram. Soc. 38, 57–66.
Schmidt, J., Altun, A.A., Schwentenwein, M., Colombo, P., 2019. Complex mullite structures fabricated via digital light processing of a preceramic polysiloxane with active alumina fillers. J. Europ. Ceram. Soc. 39, 1336–1343.
Shephard, G.C., 1999. Isohedral deltahedra. Period. Math. Hungarica 39, 83–106.
Stokes, H.T., Hatch, D.M., 1988. Isotropy Subgroups of the 230 Crystallographic Space Groups. World Scientific, Singapore, pp. 1–2.
Thomsen, C.R., Wang, F., Sigmund, O., 2018. Buckling strength topology optimization of 2D periodic materials based on linearized bifurcation analysis. Comput. Meth. Appl. Mech. Eng. 339, 115–136.
Triantafyllidis, N., Maker, B.N., 1985. On the comparison between microscopic and macroscopic instability mechanisms in a class of fiber-reinforced composites. J. Appl. Mech. 52, 794–800.
Warner, J.J., Gillies, A.R., Hwang, H.H., Zhang, H., Lieber, R.L., Chen, S., 2017. 3D-printed biomaterials with regional auxetic properties. J. Mech. Behav. Biomed. Mater. 76, 145–152.
Wu, W., Qi, D., Liao, H., Qian, G., Geng, L., Niu, Y., Liang, J., 2018a. Deformation mechanism of innovative 3D chiral metamaterials. Sci. Rep. 8, 12575.
Wu, J., Shi, Q., Zhang, Z., Wu, H.-H., Wang, C., Ning, F., Xiao, S., He, J., Zhang, Z., 2018b. Nature-inspired entwined coiled carbon mechanical metamaterials: molecular dynamics simulations. Nanoscale 10, 15641–15653.
Yourdkhani, M., Pasini, D., Barthelat, F., 2010. The hierarchical structure of seashells optimized to resist mechanical threats. Des. Nat. 138, 141–152.
Zadpoor, A.A., Hedayati, R., 2016. Analytical relationships for prediction of the mechanical properties of additively manufactured porous biomaterials. J. Biomed. Mater. Res. Part A 104A, 3164–3174.
Zhang, D., Xiao, J., Yu, W., Guo, Q., Yang, J., 2018. Hierarchical metal/polymer metamaterials of tunable negative Poisson's ratio fabricated by initiator-integrated 3D printing (i3DP). Nanotechnology 29, 505704.
Zheludev, N.I., Plum, E., 2016. Reconfigurable nanomechanical photonic metamaterials. Nat. Nanotechnol. 11, 16–22.